A Multi-Dimensional Finite Element Based Solver for Decomposing and Non-decomposing Thermal Protection Systems

Micah A. Howard[*]

Sandia National Laboratories, Albuquerque, NM, 87185, USA

Ben F. Blackwell[†]

Blackwell Consulting, Corrales, NM, 87048, USA

A multi-dimensional finite element solver for decomposing and non-decomposing ablating materials has recently been developed and is discussed in this paper. The underlying mathematical and material models are presented along with its discretization via the finite element method. The governing equations and solution algorithm is based on the one-dimensional control-volume finite element method (CVFEM) Chaleur code, a successful ablation code in use at Sandia National Labs, and this paper represents a multi-dimensional extension of Chaleur. The Equilibrium Surface Thermochemistry (EST) code, an equilibrium gas/surface thermochemistry code for decomposing and non-decomposing materials that was previously developed by the authors is used in conjunction with this new multi-dimensional ablation code to provide ablation thermochemistry information (i.e. B_c' and enthalpy tables). This new multi-dimensional ablation response code is first applied to solve two established code-to-code comparison problems with tabular aeroheating data. Another aspect of this work has been to develop the ability to couple CFD-based aeroheating data to the ablation code as a spatial and time variant boundary condition. Towards this end, we have established a one-way passing of aeroheating data from a hypersonic CFD code to the ablation code. We then examine the problem of simulating the ablation response of non-decomposing and decomposing materials in two arc-jet facilities.

Nomenclature

Roman symbols

B_c'	dimensionless ablation rate
B_g'	dimensionless pyrolysis gas transfer rate
C_H	dimensionless heat transfer coefficient
C_M	dimensionless mass transfer coefficient
$\rho_e u_e C_H$	dimensional heat transfer coefficient ($kg/s - m^2$)
$\rho_e u_e C_M$	dimensional mass transfer coefficient ($kg/s - m^2$)
$(\rho v)_w$	boundary layer mass flux ($kg/s - m^2$)
c_v	volumetric specific heat ($J/kg - K$)
D	elastic constitutive tensor
E	Arrhenius activation energy (J/kg)
e	internal energy (J/kg)
h	enthalpy (J/kg)
k	thermal conductivity ($W/m - K$) or Arrhenius pre-exponent factor (s^{-1})
M	pyrolysis gas molecular weight
$\dot{m}''$	mass flux ($kg/s - m^2$)
$\hat{n}$	unit normal
p	pressure (Pa)
$\dot{Q}$	heat source term ($J/s - m^3$ or W/m^3)

---

[*]Aerosciences Department, Senior Member AIAA.
[†]Consultant, Associate Fellow AIAA.

American Institute of Aeronautics and Astronautics

$\dot{q}''$	heat flux ($J/s - m^2$ or W/m^2)
R	gas constant ($J/kg - K$)
T	temperature (K)
t	time (s)
u	displacement (m)
v	velocity (m/s)
W	finite element test function
x	spatial coordinate (m)

Greek symbols

ϵ	dimensionless radiative emissivity or elastic strain
Γ	dimensionless volume fraction or surface of a domain
κ	permeability (m^2)
μ	dynamic viscosity ($kg/s - m$)
Ω	interior of a domain
$\dot{\omega}$	mass source term ($kg/s - m^3$)
ϕ	dimensionless porosity
ρ	density (kg/m^3)
σ	radiative Stefan-Boltzmann constant ($W/m^2 - K^4$) or elastic stress (N/m^2)

Subscripts

c	char quantity
e	boundary layer edge quantity
g	gas quantity
i, j, k, l	index notation identifiers
∞	far-field quantity
v	virgin quantity
w	wall quantity

I.   Introduction

The ability to accurately solve the detailed thermal response and surface recession of decomposing and non-decomposing materials is critical for designing the thermal protection systems of atmospheric re-entry vehicles. Several codes that solve the material thermal response of thermal protection systems have been in use for decades. The most notable is the one-dimensional CMA code[1] that was developed by the Aerotherm Corporation in the 1960s and is still in use today. Another is FIAT, a one-dimensional ablation code developed at NASA Ames Research Center and in wide use at NASA that improves upon the original CMA code.[2] The Chaleur code[3,4] is a one-dimensional control-volume finite element method (CVFEM) based code that was developed at Sandia National Labs in the mid-2000s and is currently in use at Sandia for solving material thermal response problems. ITRAC[5] is a one-dimensional code developed and in use at ATK Aerospace Systems. In the past several years, there has been an effort to extend thermal response codes such as CMA and FIAT to two and three dimensions. 3dFIAT,[6] CHAR,[7] and FEAR[8,9] are multi-dimensional codes that have been developed recently at NASA, as well as PATO[10] at UC-Santa Cruz and SAM-CEF/Amaryllis at LMS Intl. and are used for material thermal response of three-dimensional geometries. In this work, we have developed a new multi-dimensional finite element solver that is based the Chaleur algorithm and apply it to several material thermal response problems. We use the EST code,[11] an ablation thermochemistry solver, that computes the thermochemical response of the material to generate precomputed B'_c and enthalpy tables for each ablator we analyze. One challenge with the use of multi-dimensional ablation codes is the need to generate multi-dimensional, transient heating data - that is heating information with spatial and time dependence. CFD/ablation coupling has been explored in a number of efforts in the past with varying degrees of coupling.[12–15] For this work, we have developed the ability to generate aeroheating data using a hypersonic computational fluid dynamics (CFD) code. The CFD code is run at iso-thermal cold wall conditions and the corresponding heating information (typically a heat transfer coefficient, recovery enthalpy and pressure) is mapped from the CFD solution to a non-matching surface grid of the ablation sample. At this time the information passing is only one-way, meaning the CFD solution is always based on the original, un-ablated geometry and the wall temperature is always at iso-thermal cold-wall conditions (typically 293 K). For some geometries (typically features with a high radius of curvature) and non-smooth heating profiles this can lead to non-physical ablated shapes; to resolve this, a two-way CFD/ablation coupling approach is required. For other ge-

American Institute of Aeronautics and Astronautics

ometries such a arc-jet iso-q ablation samples, which have blunted shapes and are designed to have relatively uniform heat flux distributions, this one-way passage of data from the CFD code to the ablation code is valid. Nonetheless, this provides a useful means of generating aeroheating boundary conditions for multi-dimensional ablation response simulations of arc-jet samples as well as re-entry vehicles. In this paper, the governing equations for decomposing and non-decomposing ablators are presented along with our solution algorithm and several example problems are solved which highlight the capability of this new code.

II.   Governing Equations

This section presents the governing equations for decomposing and non-decomposing thermal protection materials. A decomposing material is one in which the surface recedes due to mass loss and the material pyrolyzes internally thus generating a gas that flows internally through pores in the material. A non-decomposing ablator is one in which the surface recession occurs due to mass loss but no internal material decomposition takes place. Since the governing equations for a non-decomposing ablator are a subset of the equation for a decomposing ablator we begin with a discussion of the latter set of equations.

A.   Decomposing Materials

The equations that govern the thermal response, decomposition and surface recession of a decomposing ablative material are presented in this section. Equations for conservations of energy, gas and solid mass, and pseudo-elastic mesh motion of the computational grid due to surface recession are shown here.

The energy equation, assuming thermodynamic equilibrium between the gas and solid phases, is written as

$$\frac{\partial \rho_b e_b}{\partial t} - \frac{\partial}{\partial x_i}\left(k_{ij}\frac{\partial T}{\partial x_j}\right) - \frac{\partial}{\partial x_i}\left(\rho_b h_b v_{m_i}\right) + \frac{\partial}{\partial x_i}\left(\phi \rho_g h_g v_{g_i}\right) - \dot{Q} = 0 \tag{1}$$

The terms, in the order they appear in the previous equation, correspond to the unsteady energy storage term, the conduction term, the mesh motion term, the pyrolysis gas flow term, and a volumetric energy source term.

When the material decomposes, the solid material turns into pyrolysis gases and this requires that a both a solid and gas continuity equation be defined. The mass conservation equation for the solid is written as

$$\frac{\partial \rho_s}{\partial t} - \dot{\omega}_s - \frac{\partial}{\partial x_i}\left(\rho_s v_{m_i}\right) = 0 \tag{2}$$

where the first term in the previous equation is the unsteady mass term, $\dot{\omega}$ is the solid mass source term, and the last term is the mesh motion term. Rather than solving this partial differential equation, the approach taken here is to reduce this to a set of kinetic equations which can be solved for explicitly.

If we have already subdivided the material into resin and reinforcement

$$\rho_s = \underbrace{\Gamma\left(\rho_A + \rho_B\right)}_{\text{resin}} + \underbrace{\left(1 - \Gamma\right)\rho_C}_{\text{reinforcement}} \tag{3}$$

and it is differentiated with respect to time (Γ fixed), the rate of production (or destruction) of solid is given by

$$\frac{\partial \rho_s}{\partial t} = \Gamma\left(\frac{\partial \rho_A}{\partial t} + \frac{\partial \rho_B}{\partial t}\right) + \left(1 - \Gamma\right)\frac{\partial \rho_C}{\partial t}. \tag{4}$$

The component mass source/sink terms are assumed to be given by Arrhenius equations of the form

$$\frac{\partial \rho_i}{\partial t} = -k_i \rho_{o_i}\left(\frac{\rho_i - \rho_{r_i}}{\rho_{o_i}}\right)^{\psi_i}\exp\left(-E_i/RT\right), i = A, B, C \tag{5}$$

where the subscripts o and r indicate original and residual respectively. The kinetic equations will be independently integrated to determine ρ_i which is then used in Eq. (3) to compute the solid density ρ_s.

Finally, the gas phase continuity equation is given by

$$\frac{\partial \phi \rho_g}{\partial t} - \dot{\omega}_g + \frac{\partial}{\partial x_i}\left(\phi \rho_g v_{g_i}\right) - \frac{\partial}{\partial x_i}\left(\phi \rho_g v_{m_i}\right) = 0 \tag{6}$$
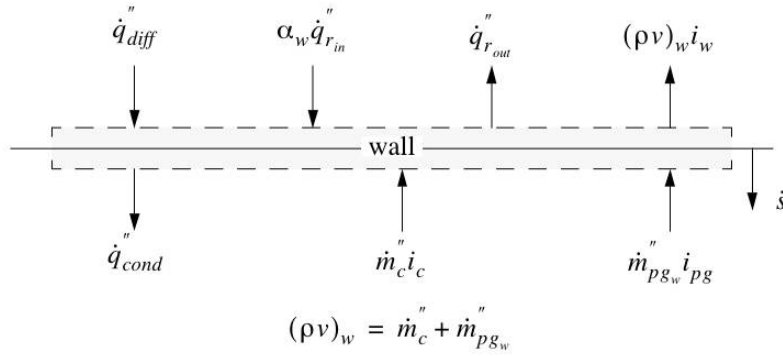
Figure 1. Energy balance on an ablating surface for a decomposing material. (Note: i is used to denote enthalpy)

where we assume in this work that the gas velocity v_{g_i} has been determined using Darcy's porous flow law and is given by

$$v_{g_i} = -\frac{\kappa}{\phi\mu} \frac{\partial p}{\partial x_i} \tag{7}$$

As the surface of the ablation sample recedes we need to move the interior nodes of the grid to new arbitrary positions in such a way that is extensible to multiple dimensions and does not lead (hopefully) to tangling of the interior elements. In order to do this, we adopt a pseudo-elastic mesh motion approach. We refer to it as pseudo-elastic because the stiffness of underlying elasticity problem is arbitrary. The surface of the ablator is displaced to a new position that is governed by the surface energy and mass balances and the interior nodal positions are simply "relaxed" into new positions. From a solid mechanics perspective, this can thought of as a prescribed displacement, static elasticity problem. The governing equation for the static elasticity problem is expressed as

$$\frac{\partial \sigma_{ij}}{\partial x_j} = 0 \tag{8}$$

where the stresses σ_{ij} are related to the constitutive tensor and the strains through

$$\sigma_{ij} = D_{ijkl}\epsilon_{kl} \tag{9}$$

and the strains are defined as

$$\epsilon_{kl} = \frac{1}{2}\left(\frac{\partial u_k}{\partial x_l} + \frac{\partial u_l}{\partial x_k}\right) \tag{10}$$

with u being a displacement field.

Equations 1, 5, 6, and 8 form the set of governing equations we need to solve to analyze the behavior of decomposing ablators. Discretization via the finite element method and the solution strategy are discussed in a later section.

1. Boundary Conditions

A sketch of the terms for the surface energy balance on an ablating surface is given in Figure 1. The control volume is of infinitesimal thickness normal to the ablating surface. The terms in the upper part of the sketch occur outside the body while those in the lower part occur inside the body. The problem is driven by a combination of the diffusive and radiation input flux terms. The term "diffusive" is used to suggest both diffusion of heat due to temperature gradients in the boundary layer as well as energy transport associated with specie diffusion to/from the ablating surface.

The surface energy balance is thus expressed as

$$\dot{q}''_{cond} = \dot{q}''_{diff} + \alpha_w \dot{q}''_{r_{in}} - \dot{q}''_{r_{out}} + \dot{m}''_c h_c + \dot{m}''_g h_g - \left(\dot{m}''_c + \dot{m}''_g\right) h_w \tag{11}$$

American Institute of Aeronautics and Astronautics

and the surface mass balance is defined by

$$\dot{m}_g^{''} - \dot{m}_w^{''} - \dot{m}_c^{''} = 0 \tag{12}$$

While convenient from a conceptual perspective, the term $\dot{q}_{cond}^{''}$ does not have to be explicitly calculated in the formulation presented here; energy balances are performed on control volumes of finite size. This term $\dot{q}_{cond}^{''}$ is a by-product of the converged system of equations. In equation 11 the "diffusive flux" is defined as

$$\dot{q}_{diff}^{''} = \rho_e u_e C_H \left(h_r - h_w \right) \tag{13}$$

which can be thought of as an aeroheating term where $\rho_e u_e C_H$ and h_r are provided by a CFD code, for instance. The input radiation term $\dot{q}_{r_{in}}^{''}$ might be from a source such as the sun or radiant lamps in which only a fraction α_w is absorbed. The output radiation term (far field radiation) is radiant exchange with the surroundings and is given by

$$\dot{q}_{r_{out}}^{''} = \sigma \epsilon \left(T_w^4 - T_\infty^4 \right) \tag{14}$$

where in this particular equation σ is the Stefan-Boltzmann constant and ϵ is the radiative emissivity of the material. For decomposing ablators, the emissivity maybe be different for virgin and charred ablator material. $\dot{m}_c^{''} h_c$ is the energy flux associated with the ablating/charing material and is defined as

$$\dot{m}_c^{''} h_c = \rho_e u_e C_M B_c' h_c \tag{15}$$

and $\dot{m}_g^{''} h_g$ is the energy flux associated with the the pyrolysis gases and is defined as

$$\dot{m}_g^{''} h_g = \rho_e u_e C_M B_g' h_g \tag{16}$$

Note that a common assumption is that heat transfer coefficient C_H and mass transfer coefficient C_M are equal. The remaining term in equation 11 is an energy transport due to mass injection (ablation plus pyrolysis gas) into the boundary layer.

2. Material Model

The material model described here is similar to the CMA model[1] with extensions for integrating the decomposition kinetics and flow through the porous char layer. The decomposing material will be modeled as a two component system: gas plus solid. Temperature dependent chemical reactions convert solid to gas and the pyrolysis gas flows through the resulting porous char layer. If ϕ is the porosity (m^3 (g)/m^3 $(s+g)$), then the bulk density ρ_b of the solid/gas mixture is given by[a]

$$
\begin{aligned}
\rho_b &= \phi \rho_g + \rho_s \\
\left[\frac{\text{Kg } (g+s)}{\text{m}^3 \ (g+s)} \right] &= \left[\frac{\text{m}^3 \ (g)}{\text{m}^3 \ (g+s)} \right] \left[\frac{\text{Kg } (g)}{\text{m}^3 \ (g)} \right] + \left[\frac{\text{Kg } (s)}{\text{m}^3 \ (g+s)} \right]
\end{aligned}
\tag{17}
$$

where the (SI) units are explicitly indicated for clarity. If the porosity $\phi|_{t=0} = 0$, we have $\rho_{o_b} = \rho_{o_s}$. It is assumed that the solid is homogeneous and that surface porosity is equal to the volume porosity.

The solid will be further subdivided into decomposing components. Phenolic based heat shield materials decompose at elevated temperatures, leaving behind a porous char matrix. Common examples include phenolic carbon, phenolic silica, and phenolic nylon. It has proven convenient to divide the material model into two components: a (phenolic) resin and a reinforcement (carbon, silica, nylon, ...). When the resin and reinforcement are mixed to provide the initial material formulation, the relative amounts of the two components can be specified by the initial resin volume fraction Γ (or mass fraction ω).

For thermal decomposition purposes, the solid density is written as

$$\rho_s = \underbrace{\Gamma \left(\rho_A + \rho_B \right)}_{\text{resin}} + \underbrace{\left(1 - \Gamma \right) \rho_C}_{\text{reinforcement}} \tag{18}$$

---

[a]In the porous flow literature, it is common to see Eq. (17) written as $\rho_b = \phi \rho_g + (1 - \phi) \rho_s$ where ρ_s would be a theoretical density and have units of Kg of solid per m^3 of solid. In the formulation presented above, ρ_s has the units of Kg of solid per m^3 of solid plus pore space. This is a density that can be measured using traditional techniques.

American Institute of Aeronautics and Astronautics

where Γ is the (known and constant) volume fraction of resin (m^3 resin/m^3 total). The two component resin model was suggested because of the presence of two dominant thermal decomposition events; if two decomposition events are inadequate to capture the physics, additional components can be added. The various "density like" terms in Eq. (3) need some further explanation. It will be helpful if the units of the individual terms in Eq. (3) are identified. This result is

$$\left[\frac{\text{Kg }(s)}{\text{m}^3\text{ (total)}}\right] = \left[\frac{\text{m}^3\text{ (resin)}}{\text{m}^3\text{ (total)}}\right]\left\{\left[\frac{\text{Kg }(A)}{\text{m}^3\text{ (resin)}}\right]+\left[\frac{\text{Kg }(B)}{\text{m}^3\text{ (resin)}}\right]\right\}+$$
$$\left[\frac{\text{m}^3\text{ }(C)}{\text{m}^3\text{ (total)}}\right]\left[\frac{\text{Kg }(C)}{\text{m}^3\text{ }(C)}\right].$$

Clearly, ρ_A and ρ_B are not densities in the classical sense because of their units; perhaps mass concentration is a more appropriate term.

If the resin mass fraction ω is specified instead of the volume fraction, then Γ is related to ω are through

$$\Gamma = \frac{\omega/\left(\rho_A+\rho_B\right)}{\omega/\left(\rho_A+\rho_B\right)+\left(1-\omega\right)/\rho_C} \tag{19}$$

The instantaneous solid state is assumed to be a weighted average of virgin material and fully charred material with the extent of reaction β being a measure of the relative distance between the virgin and char states. The extent of reaction is defined as

$$\beta = \frac{\rho_v-\rho_s}{\rho_v-\rho_c} \tag{20}$$

which leads to

$$\rho_s = \left(1-\beta\right)\rho_v+\beta\rho_c \tag{21}$$

where ρ_v is the bulk virgin density (Kg of virgin/m^3 solid) and ρ_c is the bulk char density. The initial state corresponds to $\beta=0$ while the fully charred state corresponds to $\beta=1$. At first glance, β has the appearance of a volume fraction. However, it is not a true volume fraction because virgin material and char are not states that coexist. Instead, β represents a progression from virgin to char. A corresponding "mass fraction" like variable can be defined as

$$y_v = \frac{\rho_v}{\rho_s}\left(1-\beta\right) = \frac{1-\rho_c/\rho_s}{1-\rho_c/\rho_v} \text{ and } y_c = \frac{\rho_c}{\rho_s}\beta = 1-y_v \tag{22}$$

The computational sequence will be to compute ρ_s from the decomposition kinetics (discussed below) and use Eq. (20) to compute the extent of reaction. Other solid phase material properties will be modeled as follows:

$$\phi = \phi\left(\beta\right) \tag{23}$$
$$\kappa_s = \kappa_s\left(\beta\right) \tag{24}$$
$$\left(\rho c_v\right)_s = \left(1-\beta\right)\left(\rho c_v\right)_v+\beta\left(\rho c_v\right)_c \tag{25}$$
$$\left(\rho e\right)_s = \left(1-\beta\right)\left(\rho e\right)_v+\beta\left(\rho e\right)_c \tag{26}$$

where ϕ, κ_s, $\left(\rho c_v\right)_s$ and $\left(\rho e\right)_s$ are the porosity, permeability, volumetric heat capacity and internal energy per unit volume, respectively.

The solid specific heat and internal energy can be computed from the above relationships

$$c_{v_s} = \frac{1}{\rho_s}\left[\left(1-\beta\right)\left(\rho c_v\right)_v+\beta\left(\rho c_v\right)_c\right]$$
$$c_{v_s} = y_v c_{v_v}+\left(1-y_v\right)c_{v_c} \tag{27}$$

Similarly,

$$e_s = y_v e_v+\left(1-y_v\right)e_c \tag{28}$$

where the virgin and char properties are tabulated as a function of temperature and the internal energy is computed from integrals of specific heat.

$$e_v\left(T\right) = e_{o_v}+\int_{T_o}^{T}c_{v_v}\left(T\right)dT \tag{29}$$

$$e_c\left(T\right) = e_{o_v}+\int_{T_o}^{T}c_{v_c}\left(T\right)dT \tag{30}$$

where e_o is the heat of formation at reference temperature T_o.

The bulk (gas + solid) internal energy per unit volume is

$$(\rho e)_b = \phi \rho_g e_g + (\rho e)_s \tag{31}$$

where the gas internal energy is computed from

$$e_g (T) = h_g (T) - \frac{p}{\rho_g} \tag{32}$$

where the enthalpy $i_g(T)$ is assumed known and the gas is assumed to obey the ideal gas law

$$\rho_g = \frac{p}{RT} \tag{33}$$

where R is the gas specific gas constant $(\overline{R}/M)$ and may be a function of temperature since the molecular weight may be temperature dependent. The bulk enthalpy per unit volume of the mixture is given by

$$(\rho h)_b = \phi \rho_g h_g + (\rho e)_s$$

where it is understood that $e = i$ for the solid phase.

The bulk specific internal energy is found from Eq. (31) and Eq. (17) and is given by

$$
\begin{aligned}
e_b &= \frac{\phi \rho_g}{\rho_b} e_g + \frac{\rho_s}{\rho_b} e_s \\
&= y_g e_g + (1 - y_g) e_s
\end{aligned}
\tag{34}
$$

where

$$y_g = \frac{\phi \rho_g}{\rho_b} \tag{35}$$

The bulk specific enthalpy and specific heat follow similar mixing rules

$$h_b = y_g h_g + (1 - y_g) h_s \tag{36}$$

$$c_{p_b} = y_g c_{p_g} + (1 - y_g) c_{p_s} \tag{37}$$

The enthalpy (i) of the pyrolysis gas is input in tabular form as a function of temperature. Consequently, we need to calculate e_g from h_g and the ideal gas law

$$h_g = e_g + P/\rho_g \text{ or } e_g = h_g - \bar{R}T/M(T) \tag{38}$$

where the pyrolysis gas molecular weight M is assumed to be a tabular function of T. The specific heat at constant volume of the gas phase is given by

$$
\begin{aligned}
\frac{\partial e_g}{\partial T} &= \frac{\partial h_g}{\partial T} - \frac{\bar{R}}{M} \left(1 - \frac{T}{M} \frac{\partial M}{\partial T} \right) \\
c_{v_g} &= c_{p_g} - \frac{\bar{R}}{M} \left(1 - \frac{T}{M} \frac{\partial M}{\partial T} \right)
\end{aligned}
\tag{39}
$$

For the solid thermal conductivity, the CMA model will be adopted and it is

$$k_s = y_v k_v + (1 - y_v) k_c \tag{40}$$

Other conductivity mixture rules could be readily implemented.

B. Non-decomposing Materials

Non-decomposing materials are a simplification of decomposing materials as no pyrolysis gases are generated in-depth, hence all terms involving gas energy are neglected. The governing energy equation becomes

$$\frac{\partial \rho_s e_s}{\partial t} - \frac{\partial}{\partial x_i} \left(k_{ij} \frac{\partial T}{\partial x_j} \right) - \frac{\partial}{\partial x_i} (\rho_s h_s v_{m_i}) - \dot{Q} = 0 \tag{41}$$

For a non-decomposing material this equation is solved in conjunction with the surface energy and mass balance (equations 11 and 12), less the pyrolysis gas contributions, and the mesh motion elasticity equation (equation 8).

III. Numerical Solution of the Governing Equations

The governing equations for energy and gas continuity, as well as the elastic mesh motion equation, are solved via the Galerkin finite element method. This is done by multiplying the strong form of the governing residual equations (equations 1, 5, 6, and 8) by a set of test functions W and integrating over the domain Ω. The weighted residual equations are often referred to as the weak form of the equations. When integrating by parts over the domain the so called natural boundary conditions arise over the surface Γ in the weak form. The weak form the energy equation (equation 1) for a decomposing ablator may thus be written as

$$\int_{\Omega_t} \left[W \left(\frac{\partial \rho_b e_b}{\partial t} \right) + \frac{\partial W}{\partial x_i} \cdot \left(k_{ij} \frac{\partial T}{\partial x_j} \right) - \frac{\partial W}{\partial x_i} \cdot (\rho_b h_b v_{m_i}) + \frac{\partial W}{\partial x_i} \cdot (\phi \rho_g h_g v_{g_i}) - W \dot{Q} \right] d\Omega$$
$$+ \int_{\Gamma_t} W \left(k_{ij} \frac{\partial T}{\partial x_j} \hat{n}_i \right) d\Gamma = 0 \quad (42)$$

The t subscript on Ω and Γ is added to indicate that we are performing the integration over a time varying (moving) domain. In the boundary integral term of the previous equation we recognize that

$$k_{ij} \frac{\partial T}{\partial x_j} = \dot{q}''_{cond_i} \quad (43)$$

and we can substitute the right hand side of equation 11 into equation 42 to obtain the flux terms we must integrate over the boundary (e.g. the aeroheating heat flux in equation 13).

Applying the same weighted residual methodology to the gas continuity equation (equation 6) for a decomposing ablator we arrive at its weak form, which is written as

$$\int_{\Omega_t} \left[W \left(\frac{\partial \phi \rho_g}{\partial t} \right) - W \dot{\omega}_g + \frac{\partial W}{\partial x_i} \cdot (\phi \rho_g v_{g_i}) - \frac{\partial W}{\partial x_i} \cdot (\phi \rho_g v_{m_i}) \right] d\Omega = 0 \quad (44)$$

Note that we do not perform an integration by parts on this equation (as we did for the second order spatial derivative term in the energy equation), hence no boundary integrals arise.

Lastly, the weak form of the static elasticity equation is written as

$$\int_{\Omega_t} \left[-\frac{\partial W}{\partial x_i} \cdot \sigma_{ij} \right] d\Omega + \int_{\Gamma_t} W (\sigma_{ij} \hat{n}_i) \, d\Gamma = 0 \quad (45)$$

where the boundary term $\sigma_{ij} \hat{n}_i = t_j$ is referred to as a traction force and is zero in our pseudo-elastic mesh motion system of equations.

This work uses a implicit backward difference formula (BDF) time integrator to solve the weak form of the equations in time. At each time step, we solve the nonlinear set of equations using a Newton solution strategy. This requires that we differentiate (linearize) the weak residual equations (equations 42, 45, and 44), denoted as the residual vector $\mathbf{R}$, with respect to the solution variables (the temperature T, the mesh displacement vector u_i, and the gas density ρ_g) yielding the so-called Jacobian matrix $[\mathbf{J}]$. This system of equations is solved via an iterative linear solver (typically a Generalized Minimum Residual (GMRES) method) for a solution variable update vector, denoted $\Delta \mathbf{S}$ where $\mathbf{S}$ contains the nodal temperatures, displacements, and gas densities. Written compactly, this Newton system of equations can be expressed as

$$[\mathbf{J}] \Delta \mathbf{S} = -\mathbf{R} \quad (46)$$

Once this linear system of equations has been solved for $\Delta \mathbf{S}$ we update our solution vector according to

$$\mathbf{S}^{k+1} = \mathbf{S}^k + \Delta \mathbf{S} \quad (47)$$

where k is the Newton iteration and continue linearizing and solving the Newton system of equations until the norm of the residual vector $\mathbf{R}$ drops below some small value. At this point we consider the nonlinear set of equations to be converged and continue on to the next time step.

In this work, we adopt the solution algorithm used by the Chaleur code. Chaleur segregates the energy and mesh motion equations from the gas continuity equation. That is, we solve the energy equation and elastic mesh motion equations as one coupled system to nonlinear convergence, and following this, solve the gas continuity equations to nonlinear convergence. This segregation strategy requires that we perform more than one outer sweeps through solving

American Institute of Aeronautics and Astronautics

the energy/elasticity equations and the gas continuity equations to ensure that the temperature, displacements, and gas densities are all in equilibrium at the end of the nonlinear solves. This segregation strategy and resulting outer sweeps increase the computational cost; future work is planned to develop a fully coupled solution strategy where the energy, elasticity and gas continuity equations are solved in a single set of nonlinear equations.

The numerical solution of the equations for decomposing and non-decomposing ablators has been implemented in a research code called SPARC (Sandia Parallel Aerosciences Research Code). SPARC is being developed within the Aerosciences Department at Sandia National Labs to solve computational fluid dynamics problems and material thermal response problems (ablation and heat transfer phenomena). It is fully parallel, written in C++, uses the Exodus and CGNS mesh libraries, and utilizes iterative and direct linear solvers provided by the Trilinos package[b] (also developed at Sandia National Labs).

IV. Numerical Test Problems

A. Code-to-Code Comparison Problems

Code-to-code comparison is not a part of the formal Verification and Validation process.[16] However, this does not mean that code comparisons have no place in software development. Such comparisons offer a low-level form of verification of a model, assuming the codes that are being compared against have had some level of model verification themselves. Furthermore, formal verification of proper model implementation is difficult at best for highly nonlinear ablation models, especially considering multi-dimensional geometries. In the following examples we compare the ablation code developed here (SPARC) to other established codes (Chaleur, PATO, and SAMCEF/Amaryllis).

1. Ablation Workshop 5 Test Case

This problem solves for the material decomposition and surface recession of a one dimensional specimen of the Theoretical Ablative Composite for Open Testing (TACOT) material. This example problem was created for code-to-code comparison purposes for the joint NASA/AFOSR/SNL 5th Ablation Workshop in Lexington, Kentucky from February 28-March 1, 2012. The problem was defined in the Ablation Test Case 2 document[17] and will not be repeated here. The purpose of this example is to verify that the multi-dimensional code developed here gives the similar numerical results as the one-dimensional Chaleur code that it is based on. Figures 2 and 3 show the temperature history at predefined thermocouple locations and the surface recession for the Ablation Workshop Test Case 2-2 as computed by the Chaleur code and SPARC. The reference results provided for the Workshop computed with the PATO code are also shown. These results show fairly good agreement between PATO and Chaleur. The surface temperature and first few in-depth thermocouple responses is in fairly good agreement between Chaleur and SPARC, however, the response starts to deviate for the thermocouples that are further in-depth. Furthermore, the total surface recession differs between Chaleur and SPARC by approximately $1\ mm$. The PATO and Chaleur results were generated using a ablation thermochemistry dataset provided for the Workshop and the SPARC results were computed using the EST ablation thermochemistry code. It is believed the differences in the in-depth thermocouples and the recession depth is a result of the different thermochemistry tables. Determining the true source of these differences requires further investigation and is not directly addressed in this paper.

2. Ablation Workshop 6 Test Case

This test problem builds on the previous Workshop's test problem in that in considers multi-dimensional geometries (axisymmetric and 3D iso-q samples) and uses a more sophisticated version of the TACOT material. This example problem was created for code-to-code comparison purposes for the joint NASA/AFOSR/SNL 6th Ablation Workshop at the University of Illinois Urbana-Champaign on April 10-11, 2014. The problem was defined in the Ablation Test Case 3 document;[18] readers are referred to this document for a very thorough problem description.

Figure 4 shows the surface and in-depth temperature history for the Ablation Workshop Test Case 3-0 iso-q. In this particular test, all B'_c values are zero which results in no surface recession. As can be seen in these two figures, the temperature responses between SPARC, PATO, and Amaryllis is excellent for all thermocouple locations.

Figure 4 shows the surface and in-depth temperature history for the Ablation Workshop Test Case 3-1 iso-q. This case is the same as Test Case 3-0 except now B'_c is determined by the thermochemistry tables and surface of the iso-q recedes accordingly. Here we note that temperature responses are in excellent agreement at the surface and for the
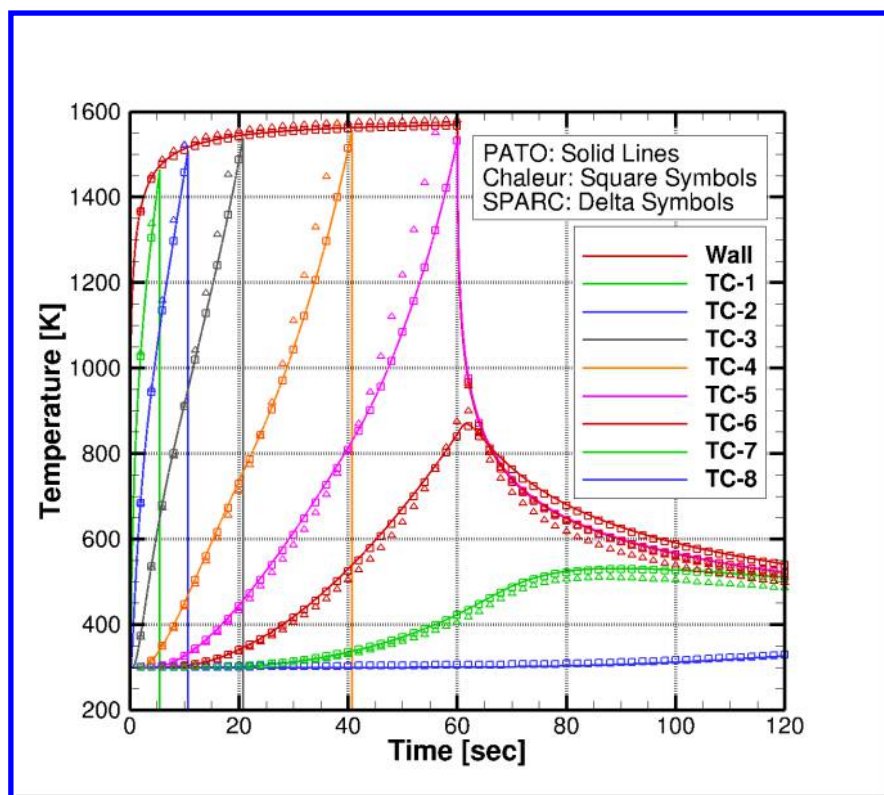
---

[b]trilinos.org

American Institute of Aeronautics and Astronautics

Figure 2. Surface temperature profiles for in-depth decomposition with surface recession.
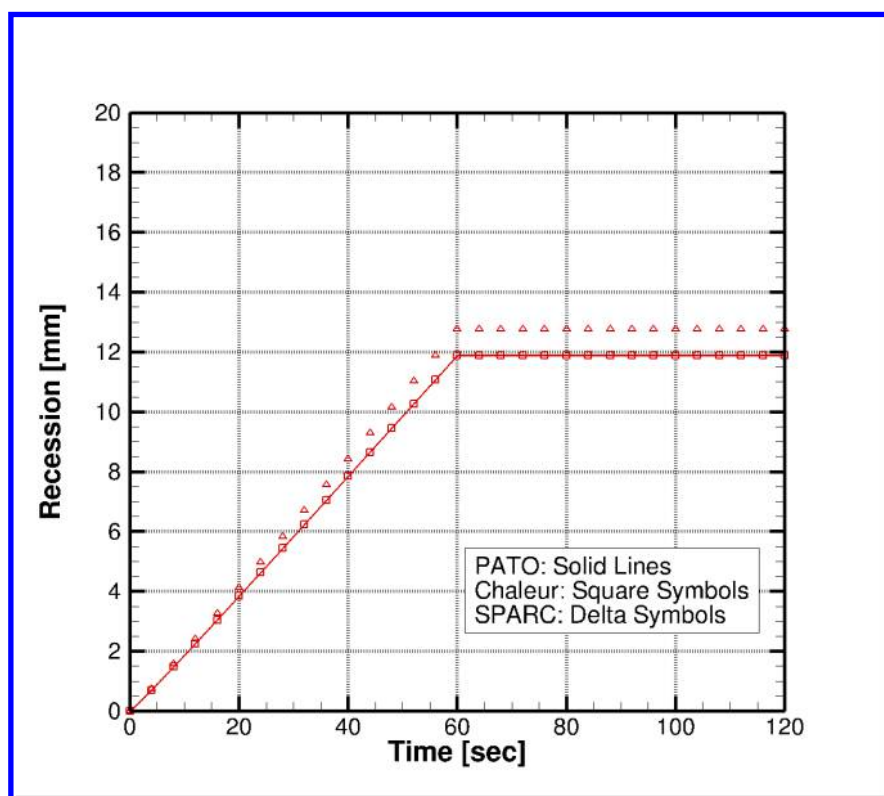
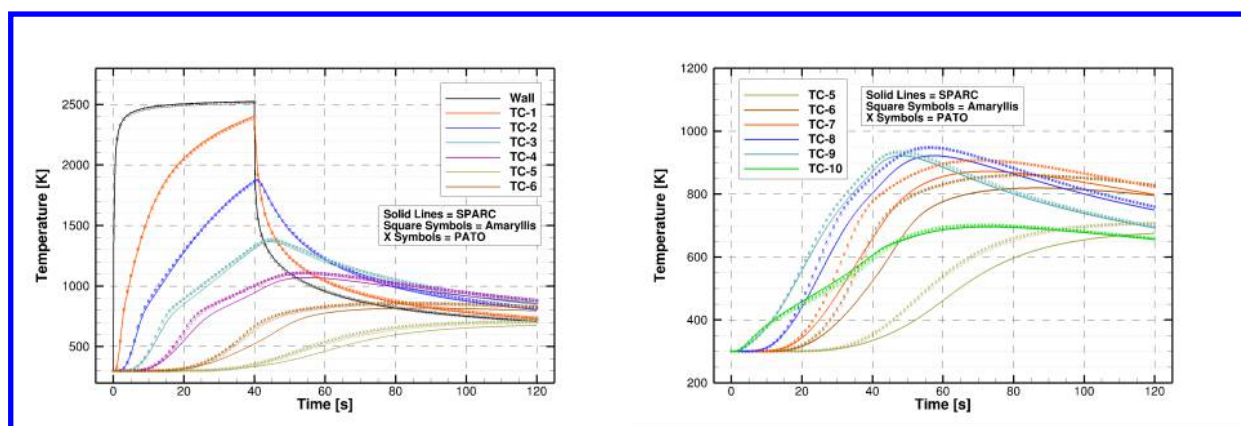**Figure 3. Surface recession profiles for in-depth decomposition with surface recession.**

American Institute of Aeronautics and Astronautics
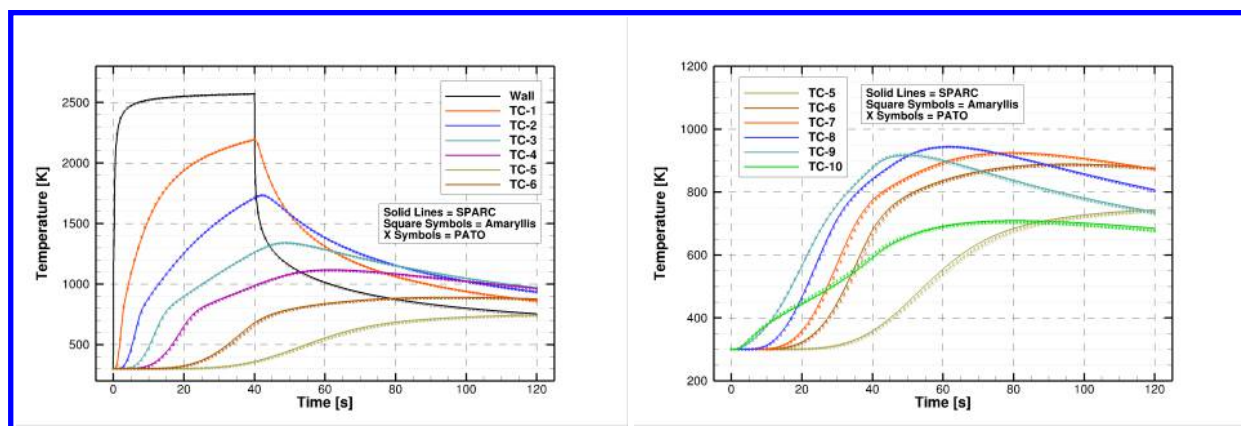
(a) Centerline thermocouples

(b) Radial thermocouples

Figure 4. Surface and in-depth temperature history for the Ablation Workshop Test Case 3-0 (non-ablating) iso-q.

(a) Centerline thermocouples

(b) Radial thermocouples

Figure 5. Surface and in-depth temperature history for the Ablation Workshop Test Case 3-1 (ablating) iso-q.

first few thermocouples. The agreement between SPARC and the other two codes starts to deviated for the more in-depth centerline thermocouples and some of the radial thermocouples. The source of these differences have not been determined at this time and requires further investigation.

Figure 6 shows the receded surface shapes of the iso-q at 10 second increments. The ablated shapes are in nearly identical between the three codes but with small differences being noticeable at the shoulder of the iso-q.

B.   Arc-Jet Ablation Problems

Have established some confidence that the governing equations are being solved correctly for decomposing materials, we now turn our attention to a more involved and realistic set of test problems. In this section, we simulate the response of graphite (a non-decomposing material) and TACOT (a decomposing material) to an arc-heated flow. We consider an axisymmetric iso-q model of each material in two of NASA Ames Research Center's arc-jets. A necessary preamble to the response of the iso-q model is a discussion on the computational fluid dynamics used to simulate the arc-heating environment. Following this, we present the numerically simulated thermal and recession response of iso-q samples to two different arc-jets.

1.   CFD Simulation of Arc-Jet Environments

Simulating the arc-jet environment is not a trivial task by any means. Much work has been devoted to learning how to perform CFD analysis of arc-jet facilities. Here we adopt much of the framework laid out by Prabhu, et al.[19,20]

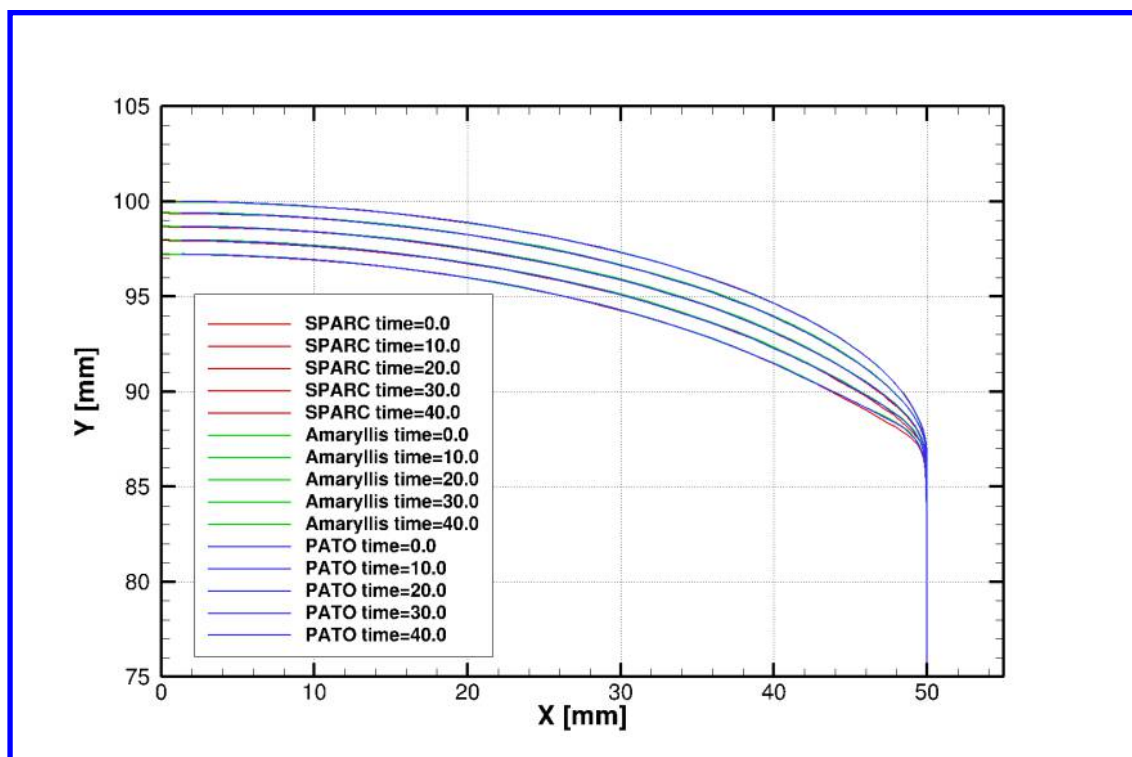American Institute of Aeronautics and Astronautics

Figure 6. Receded surface profiles for the Ablation Workshop Test Case 3-1 (ablating) iso-q.

for simulating NASA Ames Research Center's 20-MW Aerodynamic Heating Facility (AHF) and 60-MW Interaction Heating Facility (IHF).

We use US3D, a hypersonic CFD code developed at the University of Minnesota,[21] to simulate the arc-jet flow field. We make the same modeling assumptions laid out by Prabhu, et al. To summarize a few of the assumptions, we consider the flow to be laminar and in chemical and thermal non-equilibrium. We use a 6-specie (N2, O2, NO, N, O, Ar) gas model to represent the gas mixture and neglect the effects of ionization. Park's two-temperature T-Tv model is used to characterize the thermal non-equilibrium effects. As discussed by Prabhu, the flow field in the plenum of AHF is more or less uniform and results in a uniform pressure and heat flux distribution of the surface of a calorimeter in the arc-jet test section. Thus, for AHF, a uniform inflow boundary condition for the plenum is justified. This is not true for the IHF facility where the pitot pressure measurements show a uniform distribution but the heat flux measurements fit a Gaussian profile. This requires that a non-uniform inflow profile be specified for IHF CFD simulations. In this work we make a simplifying assumption and consider only uniform inflow profiles for both AHF and IHF.

Figure 7 shows the Mach contours for the AHF 7-inch nozzle with the iso-q model located 6 inches from the nozzle exit plane. The CFD grid for the AHF simulations is axisymmetric, contains roughly 67,000 cells, and converges in approximately 10,000 iterations after having ramped up to a CFL number of 10,000. Figure 8 shows the pressure and cold wall heat flux values on the surface of the iso-q model for the 7-inch nozzle of the AHF arc-jet.

Figure 9 shows the Mach contours for the IHF 6-inch nozzle with the iso-q model located 3 inches from the nozzle exit plane. The CFD grid for the IHF simulations is axisymmetric, contains roughly 66,000 cells, and converges in approximately 8,000 iterations after having ramped up to a CFL of 500. Figure 8 shows the pressure and cold wall heat flux values on the surface of the iso-q model for the 6-inch nozzle of the IHF arc-jet.

The exact inflow conditions used by Prabhu were not known when these CFD simulations were performed. However, we note that the surface pressure and heat flux profiles compare qualitatively with the profiles published by Prabhu.

2. *Thermal and Recession Response of Non-Decomposing Iso-Q Models*

Using the CFD flow field solutions for AHF and IHF we next post-process the data to obtain a cold-wall heat transfer coefficient and recovery enthalpy as well as a boundary layer edge pressure along the surface of the iso-q model.
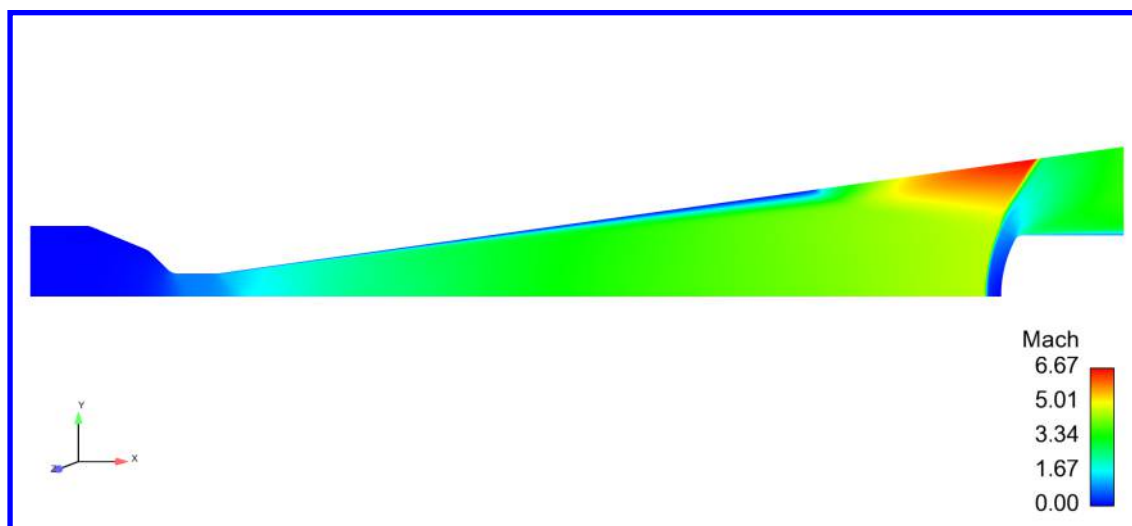
American Institute of Aeronautics and Astronautics

Figure 7. Mach number contours for the 7-inch nozzle of the AHF arc-jet.

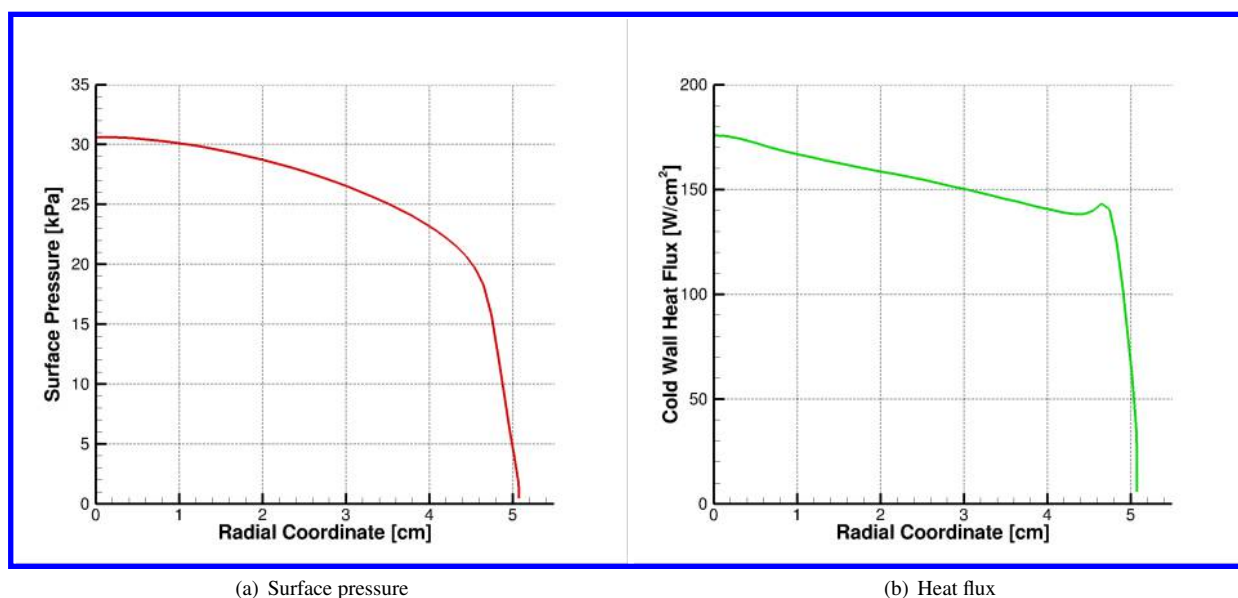(a) Surface pressure

(b) Heat flux

Figure 8. Surface pressure and cold wall heat flux profiles for the 7-inch nozzle of AHF.

To do this, we use a transfer script written to interpolate the heating data from the CFD grid to a non-node matched ablation grid. We utilize a so-called "surface transfer file" which is a grid file containing the wetted surface nodes of the ablation grid with the heating data (i.e. $\rho_e u_e C_H$, h_r, and p_e) mapped to each node. These quantities are used as spatially dependent boundary conditions for solving the thermal and recession response of the iso-q model.

An axisymmetric schematic of the material zones of a 4-inch diameter iso-q is shown in figure 11. The ablator is either a non-decomposing graphite material or a decomposing TACOT material. The model holder is LI-2200, a low conductivity insulating tile. The interface between the ablator and the insulating model holder material is assumed to be in perfect thermal contact. An air gap between the ablator and the insulator is sometimes included, however modeling the heat transfer through this air gap space is tenuous and we do not attempt to do so at this time. The mesh shown in this figure is the mesh used for the non-decomposing graphite iso-q. For a decomposing ablator, which exhibits stronger temperature and density gradients normal to the surface, the mesh is typically biased heavily toward the ablating surface; this mesh is not shown here. For all cases, the iso-q model exposure time is 60 seconds followed by a quick ($0.1\ sec$) ramp down to a cool-down period lasting 240 seconds for a total simulated duration of 5 minutes. We collect temperature histories along the centerline of the iso-q at the surface and at depths of 1, 2, 3, 4 and 5 cm.
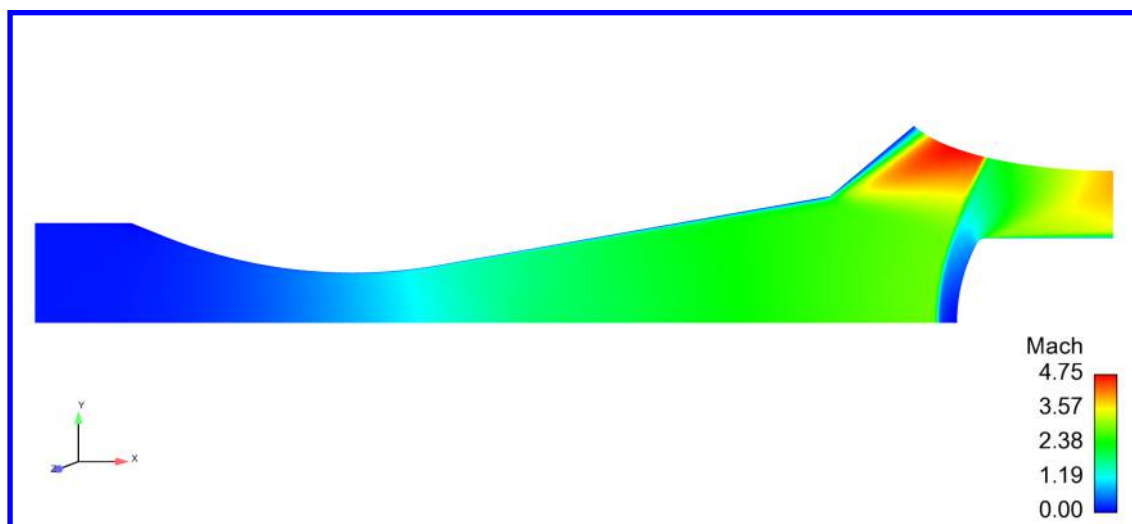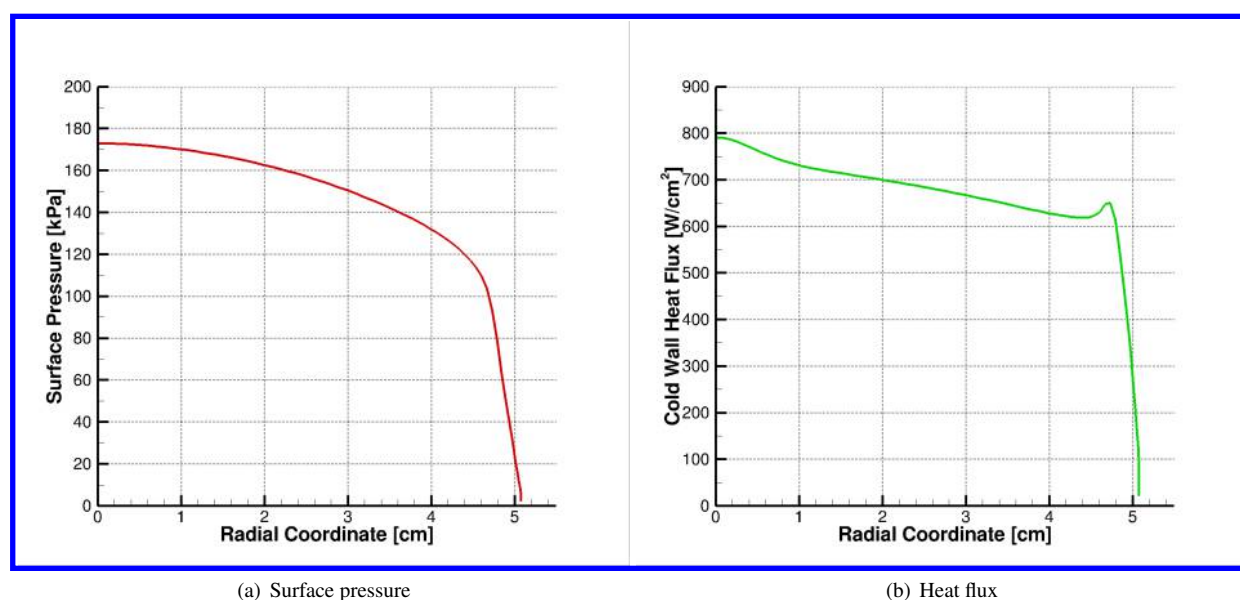
American Institute of Aeronautics and Astronautics

Figure 9. Mach number contours for the 6-inch nozzle of the IHF arc-jet.

(a) Surface pressure

(b) Heat flux

Figure 10. Surface pressure and cold wall heat flux profiles for the 6-inch nozzle of IHF.

Temperature histories are also collected along radial positions of 1, 2, 3, 4 and 5 cm from the centerline at an axial station 4 cm in from the stagnation point of the iso-q. The initial temperature of the iso-q is set to 293 K.

Figure 12 shows the temperature contours and recessed shape at the end of arc-jet exposure time (60 seconds) for a 4-inch graphite iso-q in the 7-inch AHF arc-jet. Note that, due to the relatively low heat fluxes produced in AHF and the high density of graphite, the graphite iso-q sees very little recession (less than 1 mm).

Figure 13 shows the surface and in-depth temperature history for a 4-inch graphite iso-q in the 7-inch AHF arc-jet.

Figure 14 shows the temperature contours and recessed shape at the end of arc-jet exposure time (60 seconds) for a 4-inch graphite iso-q in the 6-inch IHF arc-jet. The higher heat fluxes produced by our IHF CFD simulation yield a surface recession of 1.7 mm - still a relatively small amount of ablation. IHF is capable of producing peak cold-wall heat fluxes on the order of 2000 W/cm^2 and simulating this max facility condition may be more appropriate for producing greater recessions for high-density carbon ablators such as graphite.

Figure 15 shows the surface and in-depth temperature history for a 4-inch graphite iso-q in the 6-inch IHF arc-jet.
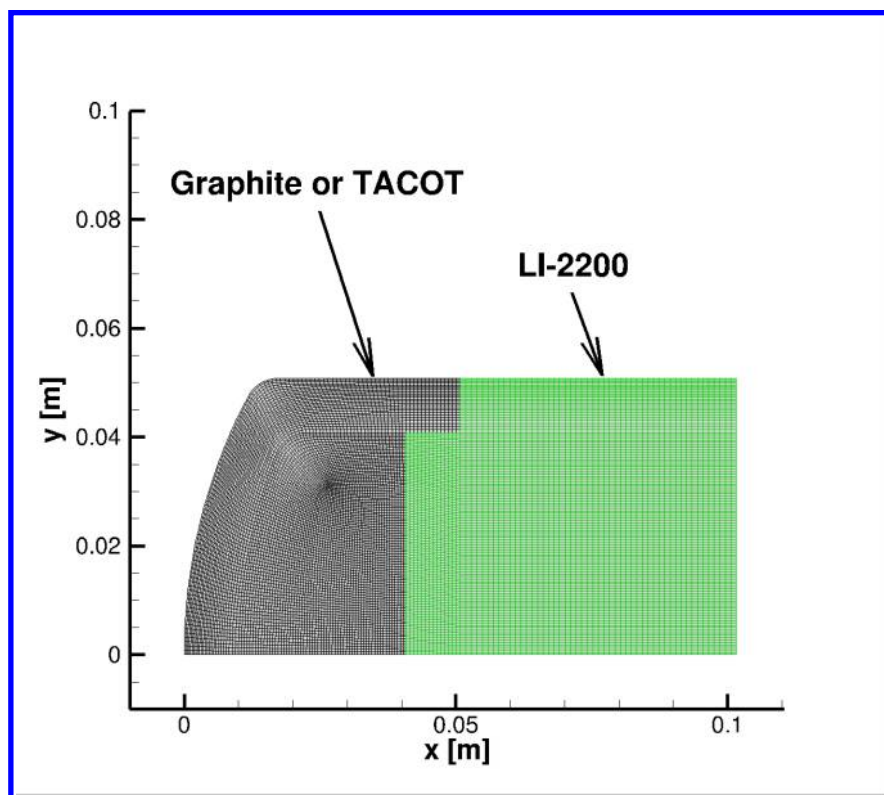
American Institute of Aeronautics and Astronautics

Figure 11. Material zones of a 4-inch diameter iso-q and the mesh used for graphite iso-q ablation simulations.

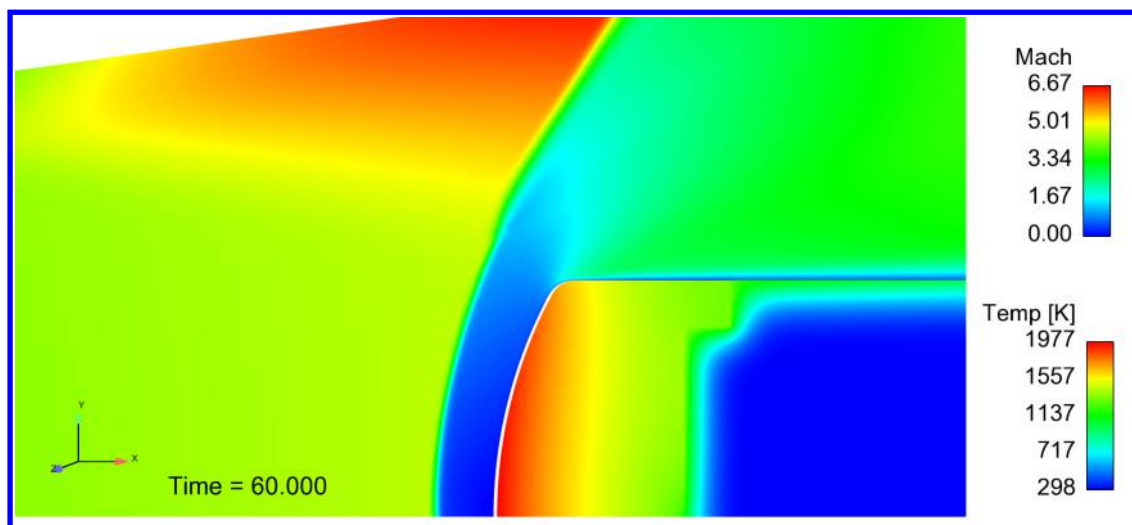**Figure 12. Temperature contours and recessed shape at 60 seconds for a 4-inch graphite iso-q in the 7-inch AHF arc-jet. The surface recession is ¿ 1 mm.**

3. *Thermal and Recession Response of Decomposing Iso-Q Models*

As with the previous example problem, the iso-q model exposure time is 60 seconds followed by a quick (0.1 sec) ramp down to a cool-down period lasting 240 seconds for a total simulated duration of 5 minutes. We collect temperature, solid density, and pressure histories along the centerline of the iso-q at the surface and at depths of 1, 2, 3, 4 and 5 cm. Temperature histories are also collected along radial positions of 1, 2, 3, 4 and 5 cm from the centerline at an

American Institute of Aeronautics and Astronautics

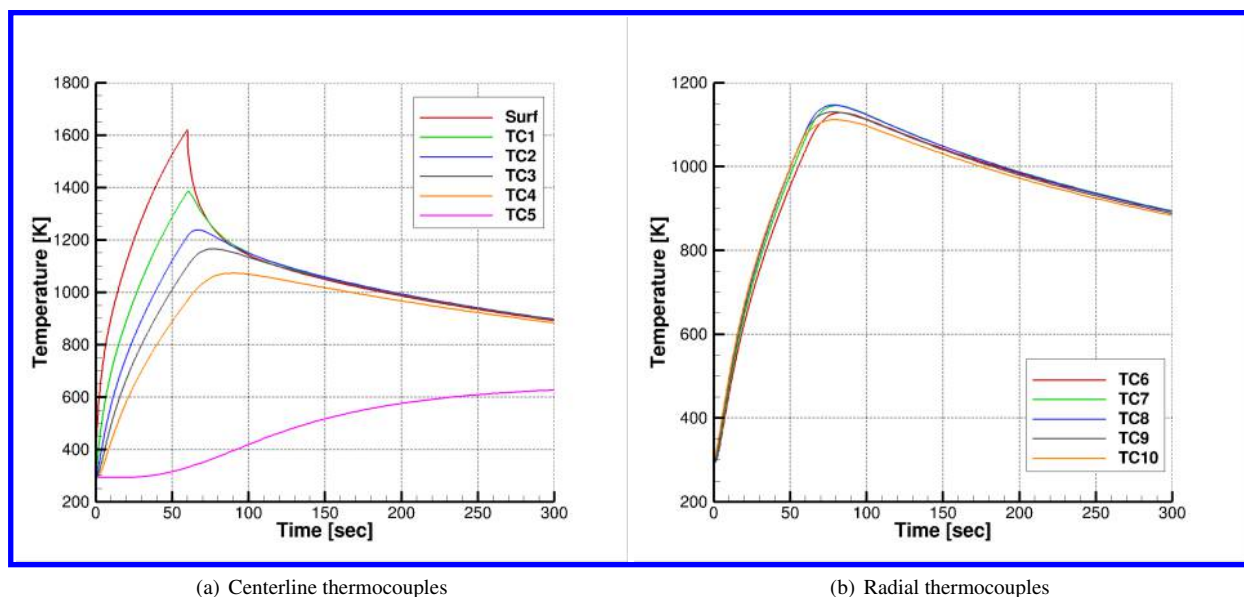(a) Centerline thermocouples

(b) Radial thermocouples

Figure 13. Surface and in-depth temperature history for a 4-inch graphite iso-q in the 7-inch AHF arc-jet.
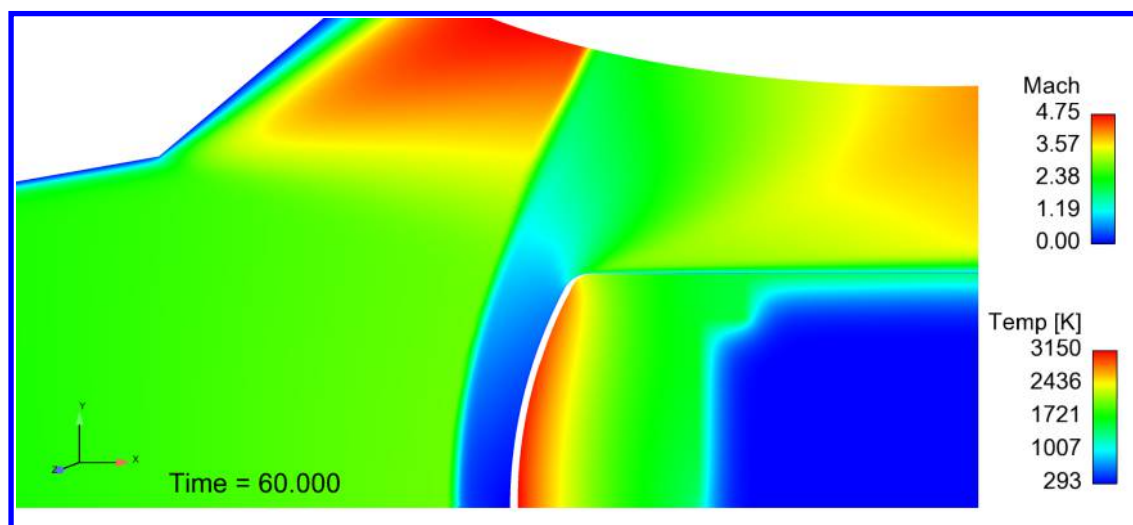

Figure 14. Temperature contours and recessed shape at 60 seconds for a 4-inch graphite iso-q in the 6-inch IHF arc-jet. The surface recession is approximately $1.7\ mm$.

axial station $4\ cm$ in from the stagnation point of the iso-q. The initial temperature of the iso-q is set to $293\ K$ and the initial pyrolysis gas pressure is set to the iso-q stagnation pressure computed by the CFD code. During the cool-down period, a uniform pressure of $1000\ Pa$ is applied to the surface of the sample.

Figure 16 shows the temperature contours and recessed shape at the end of arc-jet exposure time (60 seconds) for a 4-inch TACOT iso-q in the 7-inch AHF arc-jet. There are two interesting things to to note from this case. First, the surface recession is much greater than the recession for graphite and after 60 seconds the maximum recession is approximately $7\ mm$. Second, there is an obvious dimpling effect near the shoulder of the iso-q which is caused by the peak in the cold-wall heat flux seen in figure 8(b). This receded shape is clearly non-physical and is due to the one-way coupled nature of the CFD heating to the thermal response code. Given a two-way coupling between the CFD and ablation codes, this dimpling would not occur. Since the surface ablation is fairly large and the dimpling effect occurs at the heat flux values provided by the AHF CFD simulation we do not attempt to simulate a decomposing ablator in the IHF arc-jet, which has a much higher heating rate.

Figure 17 shows the surface and in-depth temperature history for a 4-inch graphite iso-q in the 7-inch AHF arc-jet.
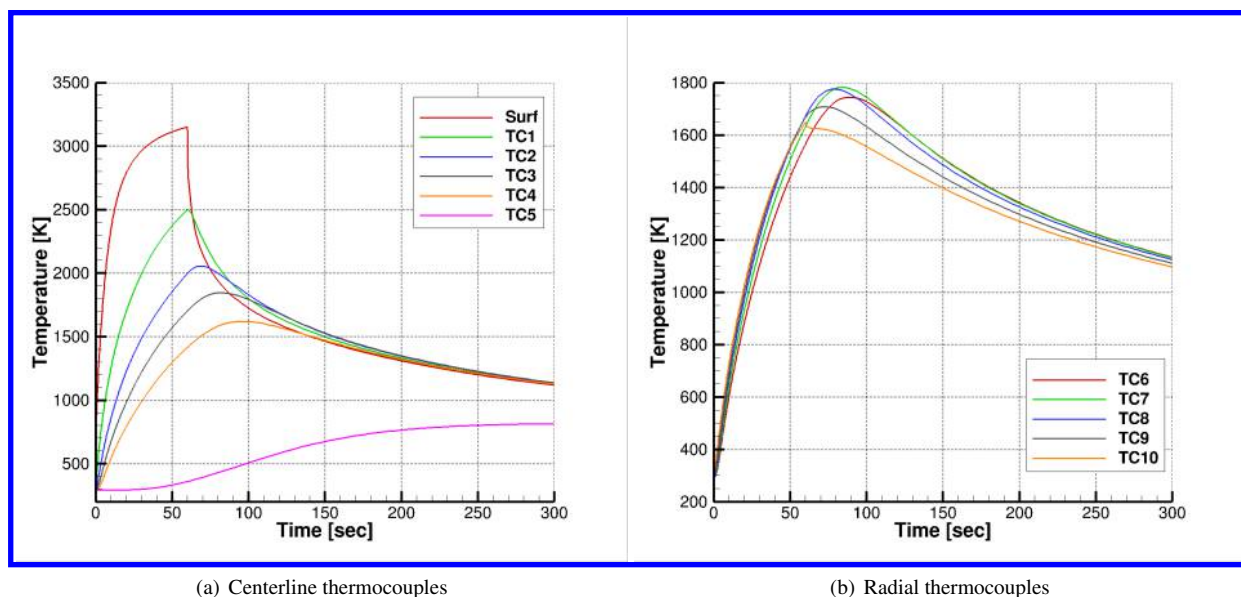
American Institute of Aeronautics and Astronautics

(a) Centerline thermocouples

(b) Radial thermocouples

Figure 15. Surface and in-depth temperature history for a 4-inch graphite iso-q in the 6-inch IHF arc-jet.
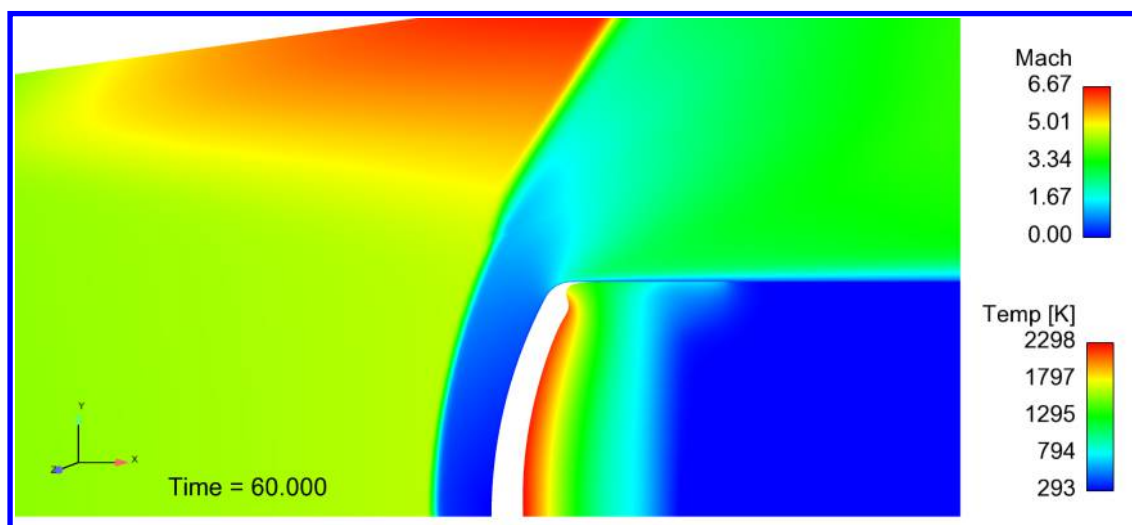

Figure 16. Temperature contours and recessed shape at 60 seconds for a 4-inch TACOT iso-q in the 7-inch AHF arc-jet.

It is interesting to note the difference in the temperature history for TC5 between graphite and TACOT, which is located within the insulating model holder material. The lower conductivity of TACOT and the in-depth decomposition of the material result in much lower temperatures of the holder material.

V.   Conclusion

The finite element method is applied to the governing equations for both decomposing and non-decomposing materials to solve for thermal response, pyrolysis gas flow, and surface recession of thermal protection materials. The algorithm used to solve these equations is the same as the one-dimensional Chaleur code (the energy equation and mesh motion equation are solved as a coupled system and the gas continuity equation is solved as segregated system), though the spatial discretization is different. The numerical solution of these governing equations has been implemented in the SPARC code. We have implemented a capability to generate aeroheating boundary conditions through a one-way
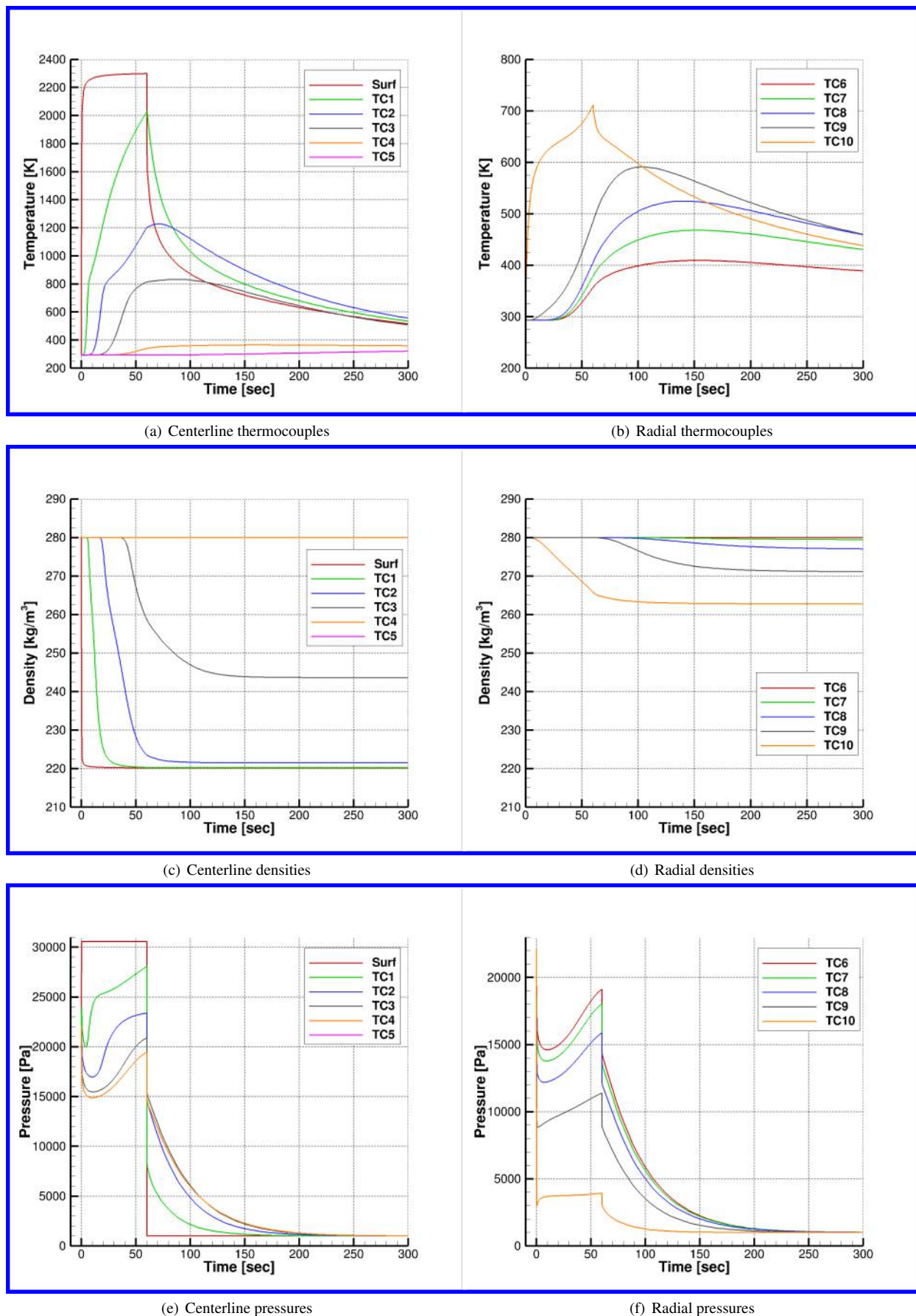
American Institute of Aeronautics and Astronautics

(a) Centerline thermocouples

(b) Radial thermocouples

(c) Centerline densities

(d) Radial densities

(e) Centerline pressures

(f) Radial pressures

Figure 17. Surface and in-depth temperature, density, and pressure history for a 4-inch TACOT iso-q in the 7-inch AHF arc-jet.

American Institute of Aeronautics and Astronautics

passing of heating data from a hypersonic CFD code the ablation solver within SPARC. Code-to-code comparisons have been made between SPARC and three other established ablation codes; the agreement between all of the codes is generally good, however we have noted some differences in temperature histories at in-depth thermocouple locations. Determining the source of these difference requires further investigation. As a step towards validation of the ablation solver within SPARC we have built a capability to simulate the flow field of arc-jets using a hypersonic CFD code and compute the resulting ablation and thermal response of an arc-jet ablation sample. Current work has focused solely on iso-q arc-jet ablation models. What is missing from this study is experimental data to validate against for openly available ablation materials. However, we have developed the framework to conduct a validation study from arc-jet data for materials of interest to Sandia National Labs. Future work is focused on developing a two-way coupled CFD/ablation analysis capability and continued effort on verification and validation of the code.

Acknowledgments

References

[1] Moyer, C. and Rindal, R., "An Analysis of the Coupled Chemically Reacting Boundary Layer and Charring Ablator, Part II, Finite Difference Solution of the In-Depth Response of Charring Materials Considering Surface Chemical and Energy Balances," Technical Report NASA CR-1061, Aerotherm Corporation, 1967.

[2] Chen, Y.-K. and Milos, F., "Ablation and Thermal Analysis Program for Spacecraft Heatshield Analysis," *Journal of Spacecraft and Rockets*, Vol. 36, No. 3, 1999, pp. 475–483.

[3] Amar, A., Blackwell, B., and Edwards, J., "One-Dimensional Ablation Using a Full Newton's Method and Finite Control Volume Procedure," *Journal of Thermophysics and Heat Transfer*, Vol. 22, No. 1, 2008, pp. 71–82.

[4] Amar, A., Blackwell, B., and Edwards, J., "Development and Verification of a One-Dimensional Ablation Code Including Pyrolysis Gas Flow," *Journal of Thermophysics and Heat Transfer*, Vol. 23, No. 1, 2009, pp. 59–71.

[5] Ewing, M., Laker, T., and Walker, D., "Numerical Modeling of Ablation Heat Transfer," *Journal of Thermophysics and Heat Transfer*, Vol. 27, No. 4, 2013, pp. 615–632.

[6] Chen, Y.-K., Milos, F., and Gokcen, T., "Validation of a Three-Dimensional Ablation and Thermal Response Simulation Code," *Proceedings of the 10th AIAA/ASME Joint Thermophysics and Heat Transfer Conference*, 28 June – 1 July 2010.

[7] Amar, A., Calvert, N., and Kirk, B., "Development and Verification of the Charring Ablating Thermal Protection Implicit System Solver," *Proceedings of the 49th AIAA Aerospace Sciences Meeting*, 4–7 January 2011.

[8] Dec, J., Braun, R., and Laub, B., "Ablative Thermal Response Analysis Using the Finite Element Method," *Journal of Thermophysics and Heat Transfer*, Vol. 26, No. 2, 2002, pp. 201–212.

[9] Dec, J. and Braun, R., "Three-Dimensional Finite Element Ablative Thermal Response and Design of Thermal Protection Systems," *Journal of Spacecraft and Rockets*, Vol. 50, No. 4, 2013, pp. 725–734.

[10] Lachaud, J. and Mansour, N., "Porous-Material Analysis Toolbox Based on OpenFOAM and Applications," *Journal of Thermophysics and Heat Transfer*, Vol. 28, No. 2, 2014, pp. 191–202.

[11] Blackwell, B. and Howard, M., "An Element Potential Based Chemical Equilibrium Solver for Gas/Surface Thermochemistry," *Proceedings of the 50th AIAA Aerospace Sciences Meeting*, 6–9 January 2012.

[12] Hassan, B., Kuntz, D., Salguero, D., and Potter, D., "A Coupled Fluid/Thermal/Flight Dynamics Approach for Predicting Hypersonic Vehicle Performance," *Proceedings of the 35th AIAA Thermophysics Conference*, 11–14 June 2001.

[13] Gosse, R. and Candler, G., "Evaluation of Carbon-Carbon Ablation Models Using a Fully Coupled CFD Solver," *Proceedings of the 40th AIAA Thermophysics Conference*, 23–26 June 2008.

[14] Nompelis, I., Candler, G., and Conti, R., "A Parallel Implicit CFD Code for the Simulation of Ablating Re-Entry Vehicles," *Proceedings of the 47th AIAA Aerospace Sciences Meeting*, 5–8 January 2009.

[15] Farbar, E., Alkandry, H., Wiebenga, J., and Boyd, I., "Simulation of Ablating Hypersonic Vehicles with Finite-Rate Surface Chemistry," *Proceedings of the 11th AIAA/ASME Joint Thermophysics and Heat Transfer Conference*, 15–20 June 2014.

[16] Roache, P., *Fundamentals of Verification and Validation*, Hermosa Publishers, Socorro, NM, 2009.

[17] Lachaud, J., Martin, A., van Eekelen, T., and Cozmuta, I., "Ablation Test-Case Series 2," Tech. rep., 5th NASA/AFOSR/SNL Ablation Workshop, 2012.

[18] van Eekelen, T., Martin, A., Lachaud, J., and Bianchi, D., "Ablation Test-Case Series 3," Tech. rep., 6th NASA/AFOSR/SNL Ablation Workshop, 2014.

[19] Prabhu, D., Saunders, D., Oishi, T., Skokova, K., Santos, J., Fu, J., Terrazas-Salinas, I., Carballo, E., and Driver, D., "CFD Analysis

American Institute of Aeronautics and Astronautics

Framework for Arc-Heated Flowfields, I: Stagnation Testing in Arc-jets and NASA ARC," *Proceedings of the 41st AIAA Thermophysics and Conference*, 22–25 June 2009.

[20]Prabhu, D., Saunders, D., Tang, C., Terrazas-Salinas, I., Carballo, E., and Driver, D., "CFD Analysis Framework for Arc-Heated Flowfields, II: Shear Testing in Arc-jets and NASA ARC," *Proceedings of the 41st AIAA Thermophysics and Conference*, 22–25 June 2009.

[21]Candler, G., Johnson, H., Nompelis, I., and Barnhardt, M., "Development of the US3D Code for Advanced Compressible and Reacting Flow Simulations," *Proceedings of the 53rd AIAA Aerospace Sciences Meeting*, 5–9 January 2015.

American Institute of Aeronautics and Astronautics